soil moisture conditions were also observed in eastern China with reported severe floods in May–June. The southern part of South America also experienced wetter-than-usual conditions, including severe flooding in Argentina and heavy precipitation in the Chilean Atacama Desert in March (see section 7c3).

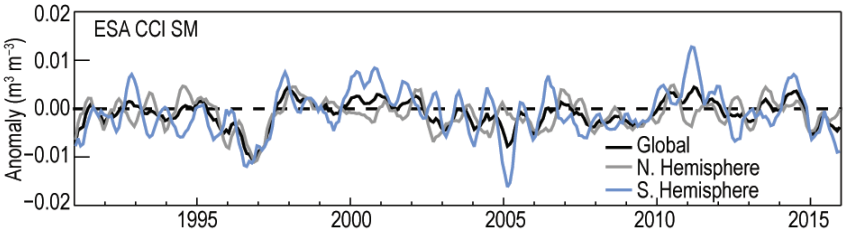


**Fig. 2.26. Time series of average global soil moisture anomalies for 1991–2015 (base period: 1991–2014). Data were masked as missing where retrievals were either not possible or of very low quality (dense forests, frozen soil, snow, ice, etc.). (Source: ESA CCI.)**

To a large extent, the spatially distinct patterns in 2015 can be related to the strong El Niño conditions during the second half of the year (NOAA/ESRL 2016). ENSO anomalies are known to potentially cause continentwide deviations in terrestrial water storages (Bauer-Marschallinger et al. 2013; Boening et al. 2012; De Jeu et al. 2011, 2012a; Miralles et al. 2014c). ENSO-driven global negative soil moisture anomalies were clear during the 1997/98 El Niño, while positive anomalies were observable for the strong La Niña episode of 2010/11, especially for the Southern Hemisphere (Fig. 2.26). The negative soil moisture anomalies in the Southern Hemisphere are visible in the time–latitude diagram (Fig. 2.27), which shows the strongest anomalies in the southern tropics. However, even though El Niño conditions in 2015 were almost as strong as in 1997/98, its impact up to the end of 2015 on global soil moisture was not as strong. This suggests that other climate oscillations may have partly counterbalanced the effects of El Niño during 2015 at least.

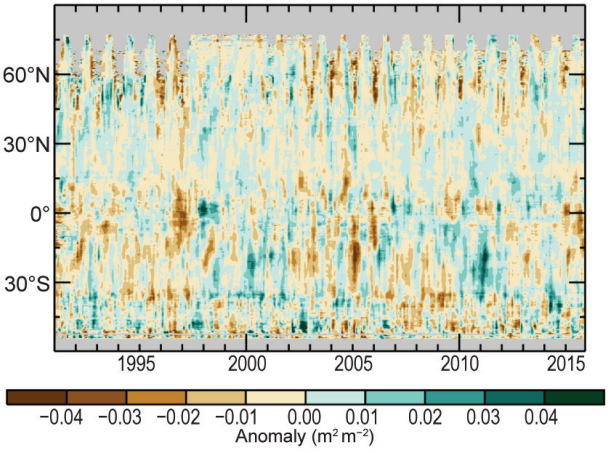


**Fig. 2.27. Time–latitude diagram of soil moisture anomalies (base period: 1991–2014). Data were masked as missing where retrievals are either not possible or of low quality (dense forests, frozen soil, snow, ice, etc.). (Source: ESA CCI.)**

No evident large-scale, long-term global soil moisture trends can be observed (Figs. 2.26, 2.27). However, this does not exclude the existence of long-term trends at the regional or local scale (Dorigo et al. 2012). Trends in average global soil moisture should be treated with caution owing to dataset properties changing over time and the inability to observe beneath dense vegetation, for mountain areas, or frozen soils (cf. gray regions in Plate 2.1f and Online Fig. S2.17).

### 9) Monitoring global drought using the self-calibrating Palmer drought severity index—T. J. Osborn, J. Barichivich, I. Harris, G. van der Schrier, and P. D. Jones

Hydrological drought results from a period of abnormally low precipitation, sometimes exacerbated by additional evapotranspiration (ET), and its occurrence can be apparent in reduced river discharge, soil moisture, and/or groundwater storage, depending on season and duration of the event. Here, an estimate of drought called the self-calibrating Palmer drought severity index is presented (scPDSI; Palmer 1965; Wells et al. 2004; van der Schrier et al. 2013a) using precipitation and Penman–Monteith potential ET from an early update of the CRU TS 3.24 dataset (Harris et al. 2014). Moisture categories are calibrated over the complete 1901–2015 period to ensure that "extreme" droughts and pluvials relate to events that do not occur more frequently than in approximately 2% of the months. This affects direct comparison with other hydrological cycle variables in Plate 2.1, which use a different baseline period. Other drought indices can give varied results (see van der Schrier et al. 2015).

van der Schrier et al. (2015) noted that 2014 appeared to have a remarkably small global area affected by drought, but the updated analysis (Fig. 2.28, with additional precipitation data that was not available at the time) now suggests that 2014 was affected by more extensive droughts (8% of land in severe drought at the end of 2014, compared with only 5% previously estimated). See Online Fig. S2.18 for a comparison with last year's analysis.

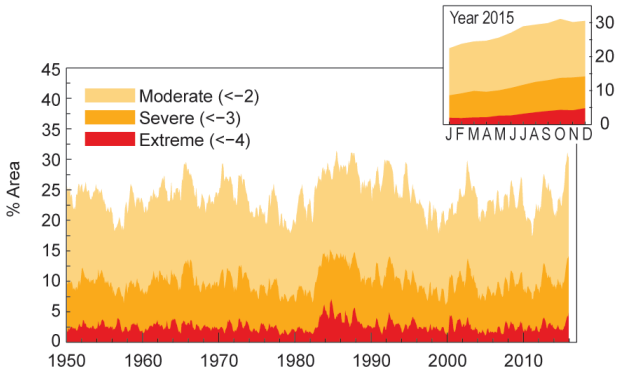


**Fig. 2.28. Percentage of global land area (excluding ice sheets and deserts) with scPDSI indicating moderate (< –2), severe (< –3) and extreme (< –4) drought for each month of 1950–2015. Inset: 2015 monthly values.**

There was a large expansion in the overall area of drought across the globe in 2015 (Fig. 2.28, inset), with 14% of global land seeing severe drought conditions (scPDSI < –3) by the end of the year. The areas where scPDSI indicates moderate (30%), severe (14%), or extreme (5%) droughts by the end of 2015 are among the highest in the post-1950 record, exceeded only by some years in the mid-1980s. The 2015 peak should be interpreted cautiously, given that more observations for the final months of 2015 will become available in due course (see Online Fig. S2.18).

The regional patterns of drought (Plate 2.1p) are partly associated with the strong El Niño event that developed during 2015. The full effect of this event may not be apparent until 2016, and other factors dominate in regions where the influence of the tropical Pacific is weak. Averaged over 2015, almost no regions of Africa experienced wet spells, and indeed most land areas south of 20°N across all continents were either near-normal (31% with scPDSI within ±1) or subject to some degree of drought (56% with scPDSI <–1).

Extensive severe or extreme drought affected many countries in southern Africa, intensifying as the 2015 El Niño progressed. These areas had been slowly recovering since a dry spell that began with the previous El Niño in 2010. In the Horn of Africa, severe drought affected Ethiopia and some neighboring regions in 2015, with significant impacts despite being apparent only over a relatively small region in the scPDSI data (Plate 2.1p). Very few areas of Africa exhibited wet spells in the 2015 mean scPDSI.

The effects of the 2014 drought in southeastern Brazil continued to be felt in 2015, though high rainfall farther south over the Paraná basin (consistent with previous strong El Niño events) replaced drought with wet conditions. New regions of drought emerged in the El Niño-sensitive regions of northeastern Brazil, Venezuela, and Colombia; these are expected to impact water supplies, hydroelectric power, and crop yields as El Niño continues into 2016. Parts of Chile remained in a severe 6-year drought in 2015 despite wetter El Niño conditions (www.cr2.cl/megasequía).

Drought conditions developed in some Central American and Caribbean nations, such as Guatemala and Haiti, contributing to food insecurity in the region. California continued to experience severe or extreme drought conditions, while most of the U.S. Midwest, South, and East were moderately or very wet, extending into Ontario, Canada.

Dry conditions were widespread across Australia, continuing from 2014. Severe or extreme drought conditions were apparent along the west coast, the southeast, and parts of Queensland, a region particularly susceptible to drought during protracted El Niño events, like the current one (section 2e1). Farther north, dry conditions were established across many parts of the Maritime Continent and parts of Southeast Asia, especially Myanmar and southwestern China (Plate 2.1p). Drought also affected parts of northern China and Mongolia in 2015 according to the scPDSI metric. In contrast with 2014, drought conditions were not evident in India despite a dry monsoon season. This was due to heavy out-of-season rainfall both early and late in the year. Dry conditions were, however, apparent over many Middle East countries.

In Europe, there was a strong contrast between the wet conditions of the southeast and Turkey and the severe drought indicated by scPDSI in eastern Europe and western Russia, affecting important crop production regions. Though not apparent in the annual-mean scPDSI (Plate 2.1p), July to December was very dry in Turkey, consistent with the strong positive North Atlantic Oscillation in late 2015 (sections 2e1, 7f).

The expansion in drought-affected areas during 2015 is similar to the earlier expansion during 1982 (Figs. 2.28, 2.29a), also a year when a strong El Niño developed, and is consistent with the reduction in the atmospheric transport of moisture from oceans to land during El Niño events (Dai 2013). The patterns of scPDSI drought (Plate 2.1p) correspond partly to those regions where El Niño events are associated with reduced rainfall (southeastern Africa, northeastern Australia, the Maritime Continent, and northeastern Brazil). There is weaker agreement with the 1997 pattern (Fig. 2.29b), which had less extensive droughts than in 2015, contributing to the absence of a clear signal in drought-affected area during the

## SIDEBAR 2.1: GLOBAL LAND EVAPORATION—D. G. MIRALLES, B. MARTENS, A. J. DOLMAN, C. JIMÉNEZ, M. F. MCCABE, AND E. F. WOOD

Evaporation of water from soils, snow-covered surfaces, continental water bodies, and vegetation (either via transpiration or interception loss) accounts for approximately two-thirds of continental precipitation. As such, land evaporation represents a key mechanism governing the distribution of hydrological resources, spanning catchment to planetary scales. The ability to monitor land evaporation dynamics is also critical in climatological applications, since evaporation 1) represents the exchange of latent energy from land to atmosphere, directly affecting air temperature; 2) influences air humidity and cloud formation, playing a strong role in driving atmospheric feedbacks; and 3) is intrinsically connected to photosynthesis, echoing changes in vegetation carbon fixation. A number of recent studies have highlighted the impact of evaporation on climate trends (e.g., Douville et al. 2013; Sheffield et al. 2012) and hydrometeorological extremes (e.g., Teuling et al. 2013; Miralles et al. 2014a).

To date, land evaporation cannot be observed directly from space. However, a range of approaches have been proposed to indirectly derive evaporation by applying models that combine the satellite-observed environmental and climatic drivers of the flux (e.g., Price 1982, Nemani and Running 1989; Anderson et al. 1997; Su 2002). Pioneering efforts targeting the global scale (Mu et al. 2007; Fisher et al. 2008) have been advanced by international activities to further explore and develop global datasets, such as the European Union Water and global Change (WATCH) project, the LandFlux initiative of the Global Energy and Water-cycle Exchanges (GEWEX) project, and the European Space Agency (ESA) Water Cycle Multi-mission Observation Strategy (WACMOS)-ET project.

Nonetheless, continental evaporation remains one of the most uncertain components of Earth's energy and water balance. Both the WACMOS-ET and LandFlux projects have brought to light the large discrepancies among widely used, observation-based evaporation datasets, particularly in semiarid regimes and tropical forests (e.g., Michel et al. 2016; Miralles et al. 2016; McCabe et al. 2016). Figure SB2.1 displays the spatial variability of land evaporation over the 2005–07 period based on data from the Penman–Monteith model that forms the basis of the official MODIS product (PM–MOD; Mu et al. 2007), the Priestley and Taylor Jet Propulsion Laboratory model (PT–JPL; Fisher et al. 2008), the Model Tree Ensemble (MTE; Jung et al. 2010), and the Global Land Evaporation Amsterdam Model (GLEAM; Miralles et al. 2011). The ERA-Interim reanalysis (Dee et al. 2011) is also included for comparison. Global estimates range between the low values of PM–MOD and the high values of ERA-Interim, with the remaining models showing a higher degree of spatial agreement.

Records of observation-based global evaporation only span the satellite era. This has not prevented a handful of studies from attempting to disentangle the impact of climate change on trends in evaporation. Jung et al. (2010) suggested a reversal in the rise of evaporation since the late 1990s, which was later shown to be a temporary anomaly caused by ENSO (Miralles et al. 2014b). Nonetheless, these studies, together with more recent contributions (Zhang et al. 2015, 2016), have indicated the existence of a slight positive trend over the last few decades, in agreement with expectations derived from temperature trends and global greening, and the theory of an accelerating hydrological cycle.

Although many of the models used for global flux estimation were originally intended for climatological-scale studies, some have evolved to provide estimates of evaporation in operational

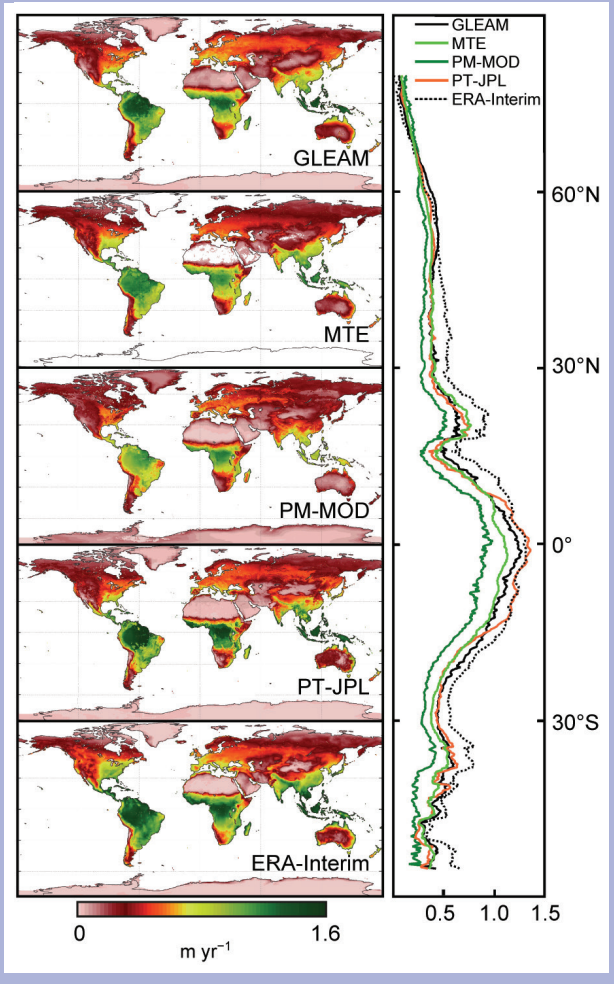


**FIG. SB2.1. Mean land evaporation patterns for different datasets. The right panel illustrates the latitudinal averages over the 2005–07 period. Adapted after Miralles et al. (2016).**

mode, with ongoing efforts aiming to reduce product latency and improve spatial resolution. This opens up a range of possible applications, from global drought monitoring to irrigation management. Some examples of evaporation datasets targeting near-real-time simulation at continental scales include the Land Surface Analysis Satellite Applications Facility (LSA SAF) product (Ghilain et al. 2011) and the Atmosphere–Land Exchange Inverse (ALEXI) datasets (Anderson et al. 1997, 2011). While GLEAM was not deliberately designed with an operational intent, the current version 3 dataset has been updated to include 2015, using observations from the Soil Moisture and Ocean Salinity (SMOS) mission (www.gleam.eu). Figure SB2.2 shows the anomalies in evaporation for 1980–2015 based on this new dataset.

Periods of global decline in evaporation typically coincide with El Niño conditions, and are associated with drought in the water-limited ecosystems of the Southern Hemisphere (Miralles et al. 2014b). The year 2015 was no exception: despite El Niño conditions intensifying only in the second half of 2015, Fig. SB2.2 shows anomalously low evaporation in central Australia, eastern South America, Amazonia, and southern Africa. Considering the entire multidecadal record, the continental evaporation in 2015 does not seem particularly anomalous, as climate variability is superimposed on a positive trend of ~0.4 mm $yr^{-1}$. For most of the Northern Hemisphere, evaporation was above the multidecadal mean, with the notable exception of California, which experienced extraordinary drought conditions.

With the development of improved algorithms dedicated to estimating evaporation from satellite observations, global operational monitoring of land evaporation is becoming a realistic proposition. While discrepancies amongst current models are still large (Michel et al. 2016; McCabe et al. 2016), several of the existing datasets compare well against each other and against in situ measurements. These datasets open new pathways to diagnose large-scale drought and irrigation needs, and to improve water resources management and the characterization of hydrological cycles. Satellite-based evaporation estimates respond to long-term changes in Earth's water and energy budgets and are able to capture fluctuations due to internal climate variability. The mean distribution of evaporation anomalies in 2015 (Fig. SB2.2) is a clear example of the underlying effects of multidecadal climate trends and climate oscillations on the terrestrial water cycle.

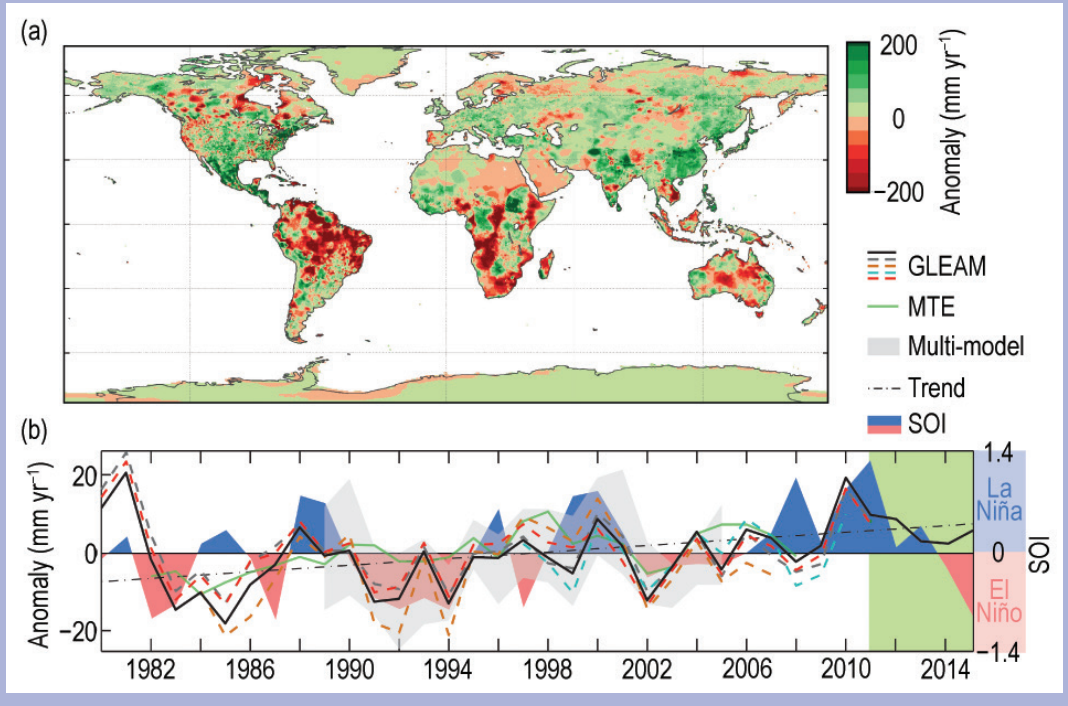


**Fig. SB2.2. (a) 2015 land evaporation anomalies. (Source: GLEAM). (b) Mean continental evaporation anomaly time series for the satellite era, based on an ensemble of GLEAM datasets (after Miralles et al. 2014b). The MTE dataset (Jung et al. 2010), the satellite-based multimodel range by Mueller et al. (2013), and the Southern Oscillation index (SOI) are also shown. GLEAM runs for 2012–15 incorporate SMOS data. Anomalies are calculated relative to the 1997–2007 period in which all datasets overlap.**

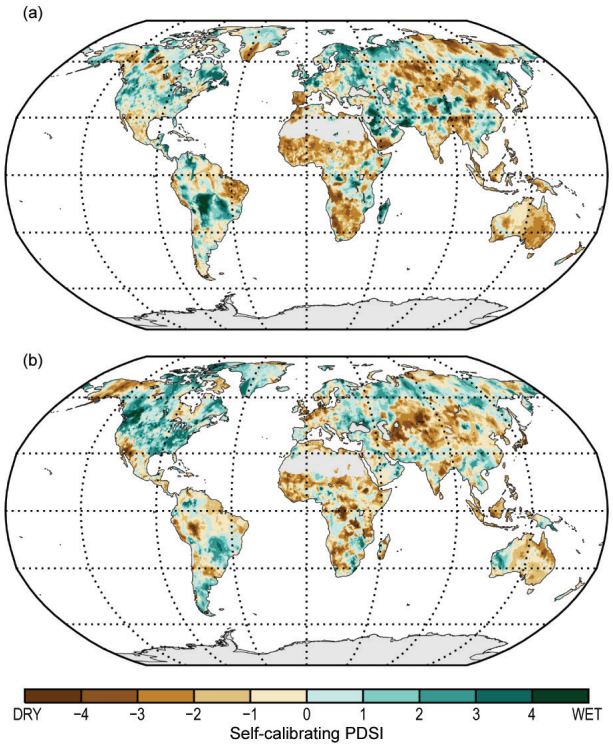


**Fig. 2.29. Mean scPDSI for (a) 1982 and (b) 1997, years in which a strong El Niño developed. No calculation is made (gray areas) where a drought index is meaningless (e.g., ice sheets and deserts with approximately zero mean precipitation).**

strong 1997/98 El Niño (Fig. 2.28). Indeed, the other post-1950 years with scPDSI drought areas as large as in 2015 (31% in moderate drought; e.g., 1985 and 1987) have quite different spatial patterns (Online Fig. S2.19), with severe drought in the Sahel and India, for example; 1985 was not a strong El Niño while 1987 was part of the long 1986/87 event.

### e. *Atmospheric circulation*

#### 1) Mean sea level pressure and related modes of variability—R. Allan and C. K. Folland

Mean sea level pressure (MSLP) provides diagnostics of the major modes of variability that drive significant weather and climate events (Kaplan 2011). Arguably, the most globally impactful mode is the El Niño–Southern Oscillation (ENSO), for which the sea level pressure-derived Southern Oscillation index [SOI; Allan et al. 1996; normalized MSLP difference between Tahiti and Darwin (various other indices are also commonly used); Kaplan 2011; section 4b] is an indicator. For 2015, the SOI was negative, indicating the presence of the strongest El Niño since 1997/98 (see Sidebar 1.1).

The SOI trace since 2009 highlights the shift from El Niño to strong La Niña conditions around mid-2010, continuation as a protracted La Niña (with cold SST anomalies in the Niño-4 region) until its demise in early 2012, and then near-normal conditions until early 2013. Mainly positive (La Niña–type) values followed until a swing to negative (El Niño–type) conditions since early 2014 (Fig. 2.30; with warm SST anomalies in the Niño-4 region). Apart from April and May 2014, the SOI was negative from February 2014 onwards (Fig. 2.30). Accordingly, the Niño-3 and 4 regional SST anomalies have been positive since April and February 2014 respectively (section 4b). Following Allan and D'Arrigo (1999), by these measures this constitutes a protracted El Niño episode: "*….periods of 24 months or more when the SOI and the Niño 3 and 4 SST indices were of persistently negative or positive sign, or of the opposite sign in a maximum of only two consecutive months during the period….*" Figure 2.30 shows the presence of these protracted El Niño and La Niña episodes in the SOI record since 1876, demonstrating that they can last up to six years (e.g., the 1990–95 protracted El Niño; see Gergis and Fowler 2009).

Major El Niño and La Niña events can be near-global in their influence on world weather patterns, owing to ocean–atmosphere interactions across the Indo-Pacific region, with teleconnections to higher latitudes in both hemispheres. Protracted El Niño and La Niña episodes tend to be more regional in

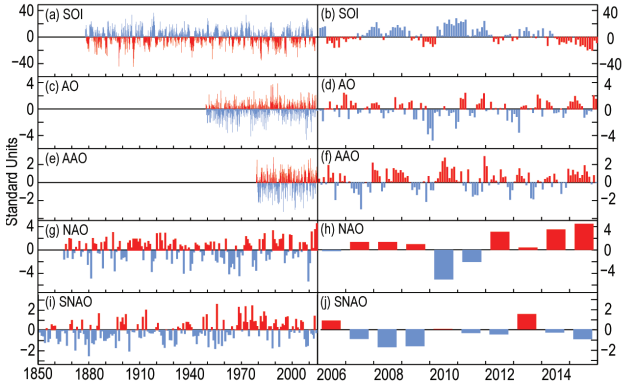


**Fig. 2.30. Time series for modes of variability described using sea level pressure for the (left) complete period of record and (right) 2006–15. (a),(b) Southern Oscillation index (SOI) provided by the Australian Bureau of Meteorology; (c),(d) Arctic Oscillation (AO) provided by NCEP Climate Prediction Center; (e),(f) Antarctic Oscillation (AAO) provided by NCEP Climate Prediction Center; (g),(h) Winter (Dec–Feb) North Atlantic Oscillation (NAO) average provided by NCAR (presented for early winter of each year so winter 2015/16 is not shown); (i),(j) Summer (Jul–Aug) North Atlantic Oscillation (SNAO) average (Folland et al. 2009).**